ICAS-98-2,1,4

A98-31492

EXPERIMENTAL AND NUMERICAL INVESTIGATIONS ON WAVERIDERS IN DIFFERENT FLIGHT REGIMES

D. Hummel, R. C. Blaschke

Institute of Fluid Mechanics, Technical University Braunschweig, Germany

Th. Eggers, D. Strohmeyer

Institute of Design Aerodynamics, DLR Braunschweig, Germany

Abstract

A waverider configuration named DLR–F8 has been generated at $M_\infty^\star = 12.0$ with practicable distributions of camber and volume. The investigations on this geometry comprise both experimental and numerical studies in the whole flow regime from subsonic up to hypersonic Mach numbers.

In hypersonic flow the performance characteristics remained constant in a wide range of Mach numbers. If the shock detaches from the leading edge L/D increases by expansion flow or by leading edge vortices on the upper surface. The leading edge bluntness can be minimized in order to avoid a significant increase of wave drag and thermal loading can be handled by a proper combination of material and structural design.

In the transonic flow regime the highest L/D is achieved. The performance characteristics are dominated by leading edge vortices on the upper surface, and the movement of the terminating shock leads to considerable changes in the centre of pressure position.

In incompressible flow a complex vortex structure exists on the upper surface which is distinctly different from that on delta wings. In the vortex centre exists a region of reduced velocity which is due to the leading edge curvature in the front part of the waverider.

The Euler and Navier–Stokes codes used in the present studies are powerful tools to predict the flow around the configuration in the whole Mach number range.

1. Introduction

The waverider principle for the design of hypersonic vehicles is well–known since a long time [1], [2]. The exact solutions for the inviscid basic flow past wedges and cones can be used to design simple flowfields around 3D bodies with shocks attached to the leading edges, with the basic flow on the lower side and with the free stream flow on the upper side. If the methods for inviscid flow are combined with a boundary layer analysis and an optimization routine, so-called viscous optimized waveriders [3], [4] turn out which yield high L/D values and in some cases also reasonable volume and camber distributions.

In recent studies of the waverider principle the basic flow on the lower side taken from a cone has been replaced by the 3D flow in the vicinity of a shock wave with a given shock angle and an arbitrarily shaped cross section [5], [6]. For small crossflow components the 3D lower surface flowfield can be calculated from locally conical flows related to osculating cones with constant values of the cone angle and the shock strength but with different cone lengths depending on the local shock curvature in the cross section. On this basis the possibilities to design waverider configurations and to meet constraints for practical applications have been enlarged greatly.

Further studies of the waverider principle have been carried out in a close cooperation between DLR Braunschweig (Institute of Design Aerodynamics) and TU Braunschweig (Institute of Fluid Mechanics and Institute of Aircraft Design and Structure Mechanics) [7]. Using the interactive computer code WIPAR [6], [8], [9] baseline configurations for realistic vehicle shapes have been created, and volumetric requirements for the integration of structures, fuel, systems and payload for various missions [10], [11] have been taken into account. The Euler/Navier-Stokes code CEVCATS [12], [13] as well as experimental data in hypersonic flow [7] have been used to validate [14] the design tool WIPAR and the surface inclination method SOSE [15]. For practical applications the free stream upper surface of the waveriders has been replaced by an expansion contour in order to create a wing body configuration with trailing edge flaps. Comprehensive studies on the off-design behaviour of waveriders have been carried out in supersonic [16], [18] as well as in transonic and subsonic flow [17], [18]. The effects of leading edge bluntness have also been studied [18]. Recent optimizations of the performance data in the subsonic and transonic flow regime lead to planforms with a highly swept front part and a rear part with moderate sweep [18], [19].

In the course of these investigations the geometry of a realistic waverider configuration DLR-F8 has been designed [16] and a windtunnel model has been built. This configuration has been studied quite intensively by means of numerical simulations with various methods as well as by measurements in the $1 \times 1 \, m^2$ Transonic Windtunnel of DLR Göttingen and in the 1.3 m Low Speed Windtunnel of TU Braunschweig[†]. Experiments in the Hypersonic Windtunnel of DLR Köln are still in progress. In the present paper results for this waverider configuration will be presented for the whole flight regime from hypersonic to incompressible flow.

2. Notations

$A = b^2/S$	Aspect ratio
$C_D = \frac{D}{q_\infty S}$	Drag coefficient
$C_{D,f} = \frac{D_f}{q_\infty S}$	Friction drag coefficient
$C_L = \frac{L}{q_\infty S}$	Lift coeficient
$C_{m25} = \frac{M_{25}}{q_\infty S l_\mu}$	Pitching moment coefficient based on N_{25}, nose–up positive
$C_{l,x} = \frac{dL}{q_\infty S}$	Local cross sectional lift coefficient
$C_g = \frac{g - p_\infty}{q_\infty}$	Total pressure coefficient
$C_p = \frac{p - p_\infty}{q_\infty}$	Static pressure coeficient
D	Drag
L	Lift
$M_\infty = \frac{U_\infty}{a_\infty}$	Mach number
M_{25}	Pitching moment based on N_{25}
N_{25}	Geometric neutral point
$R_\infty = \frac{U_\infty l}{\nu_\infty}$	Reynolds number
S	Planform area
T_W	Wall temperature
U_∞	Free stream velocity
V	Volume
a_∞	Free stream speed of sound
$b = 2s$	Wing span
g	Local total pressure
l	Root chord
l_μ	Reference chord
p	Local static pressure
q	Local dynamic pressure
r_N	Nose radius
$s = b/2$	Wing semispan
t	Wing tip chord
x, y, z	Body–fixed coordinates according to Fig. 3
x_{CG}	Centre of gravity position
x_N	Aerodynamic centre position
$x_{N_{25}}$	Geometric neutral point position
x_P	Centre of pressure position
y_1	Local semispan
α	Angle of attack
α_0	Zero angle of attack
η	Volumetric efficiency
$\lambda = l/t$	Taper ratio
ν_∞	Kinematic viscosity
σ	Shock angle

Sub– and superscripts

∞	Free stream
$*$	Design
c	Cruise
f	Friction
i	Inviscid
v	Viscid

3. Design and analysis methods

A brief description of the design and analysis methods used in the present work is given here.

3.1 Design method

The geometry of a waverider is generated for a certain Mach number M_∞^*. In a cross section through the flowfield at the end of the configuration an arbitrarily shaped shock with constant strength is prescribed. For the flow in the vicinity of this shock small cross-flow components are assumed and the local flowfield in planes normal to the shock is replaced by the flow past a circular cone. The length of this cone is given by the local curvature of the prescribed shock and it varies therefore over the span. Thus a 3D shock wave is generated by osculating cones with different lengths and constant values of cone angle, shock angle and shock strength. Design parameters are Mach number M_∞^*, shock angle σ and shock shape in the cross section at the rear end of the configuration.

Once the shock shape is specified the leading edges of the waverider can be prescribed on the shock surface in order to meet a certain planform. In each plane normal to the shock wave the streamline through

the leading edge according to the well-known exact Taylor-Maccoll solution marks the lower surface of the waverider, and its shape and corresponding pressure distribution turn out simultaneously. If the upper surface is chosen as a free stream surface starting from the leading edge, the waverider geometry as well as its aerodynamic characteristics in inviscid flow are known.

The code WIPAR allows fully interactive input of all geometric and flow parameters and the resulting geometries and aerodynamic performance data are displayed immediately. Viscous effects are taken into account by a boundary layer analysis, and for the design of the upper surface of the waverider options exist to apply flow expansion or compression [5], [6], [8], [9].

3.2 Euler/Navier-Stokes calculations

Numerical solutions of the Euler and the Navier-Stokes equations for waverider configurations have been obtained with the DLR codes CEVCATS [12], [13] and FLOWER [20]. For subsonic and transonic flows code versions with central differencing and artificial dissipative terms [12], [20] have been used and supersonic and hypersonic flows were computed with upwind flux vector splitting for spatial differencing [13]. In all versions the numerical solution is advanced in time by explicit multistage time stepping schemes. Convergence to the steady state is accelerated by local time stepping, implicit residual smoothing, enthalpy damping and a multigrid algorithm. The codes CEVCATS and FLOWER are developped for arbitrary multiblock structured computational domains. The compressibility effects are calculated by assuming either calorically perfect gas or air in thermochemical equilibrium. Concerning viscous effects the Navier-Stokes versions of the codes are able to treat laminar flows as well as turbulent flows using the Baldwin-Lomax and the $k-\omega$ turbulence models.

Euler solutions have been used to check the validity of the assumptions in the design code WIPAR and to analyse the off-design behaviour of waveriders on the basis of calculations for inviscid flow. The Navier-Stokes calculations have been carried out to get some master solutions for viscous flows, which are compared with experimental results and which indicate the validity of boundary layer assumptions.

4. Configurations

For the present investigations a waverider configuration has been designed and a windtunnel model has been built. Its geometric shape is described subsequently.

4.1 Basic configuration

Using the interactive code WIPAR a waverider configuration has been generated at a Mach number $M_\infty^* = 12.0$. The prescribed shock angle was $\sigma = 9.1°$.

The shock shape in the cross section at the rear end of the configuration may be taken from Fig. 1. The planform consists of a rounded and highly swept front part and a rear part with slightly reduced sweep. The lower surface results from the Taylor-Maccoll solutions for the various osculating cones and the upper surface has been chosen as a free stream contour through the leading edges. This basic design is named WRE 12.0-IFL.

Predesign studies [8] had shown that for a given planform and increasing shock angle the thickness of the resulting waverider increases whereas the obtainable lift to drag ratio decreases. Therefore, the present design is a compromise between the necessary volume for a certain mission with a volumetric efficiency $\eta = V^{2/3}/S = 0.152$ and an obtainable lift to drag ratio in inviscid flow $(L/D)_i = 10.21$. The planform shape has been chosen in such a way that the usable volume is concentrated near the centre line of the configuration. In addition the position of the centre of pressure is located close to the centre of gravity and hence the configuration can be trimmed. The waverider WRE 12.0-IFL meets all constraints for a hypersonic cruise mission at $M_{\infty c} = 4.5$. The large difference between the cruise Mach number $M_{\infty c}$ and the Mach number M_∞^* at which the waverider geometry has been generated is due to the fact that high Mach numbers M_∞^* lead to small cross section curvatures and this allows a proper integration of fuel, tanks, systems and payload. Therefore, the cruise of such waveriders takes place at "off-design" conditions, but comprehensive predesign studies [18] have shown that the obtainable lift to drag ratio is almost independent of Mach number in a wide range $M_\infty < M_\infty^*$. The geometric parameters as well as the aerodynamic performance data of the basic waverider configuration WRE 12.0-IFL are given in Tab. 1. All data related to this configuration result from the design code WIPAR.

4.2 Modified configuration

Due to the free stream upper surface a large base area occurs at the rear end of the configuration which produces additional drag throughout the whole flight regime. The central part of this base area can be used for the integration of the nozzles of the propulsion system and in the outer part of the configuration the free stream flow can be replaced by an expansion flow in order to generate an upper surface which meets the rear end of the configuration at a sharp trailing edge. Using these ideas the waverider WRE 12.0-IFL has been modified.

The necessary nozzle area on the base of the body has been determined according to [11]. The wing tips were cut in order to achieve a constant flap chord which leads to a taper ratio of $\lambda = 0.05$. Between the nozzle area and the new wing tip a sharp trailing edge was defined which consists of two straight parts for the installation of ailerons and an elevator both with

3

straight hinge line. The endpoints of trailing edge segments were located on the original lower waverider contour. On the lower side only relatively slight modifications of the original waverider contour were necessary to meet this new trailing edge. On the upper side an expansion surface was formed in the outer portions by means of cubic splines with smooth transitions to the original waverider contour. The mean inclination of the new upper surface against the free stream is 1 : 7 which coincides with the lift to drag ratio in viscous flow. In order to maintain a proper volume distribution the original waverider contour remained unchanged in the regions in front of the dashed line indicated in Fig. 2. In the inner portion of the configuration a square–shaped fuselage is formed with some boattailing in lateral and vertical direction to meet the nozzle area at the base. Finally the edges of the resulting body were rounded with variable radii. The modified configuration is named DLR-F8, see Fig. 2, and some geometric data may be taken from Fig. 3 and Tab. 1.

The modified waverider configuration was subject to detailed numerical and experimental investigations. Some details of these are described subsequently.

4.3 Numerical investigations

In the aerodynamic analysis the propulsion box and the nozzle are not modeled. The propulsive jet is represented by a solid sting with constant cross section which extends far downstream up to the edge of the computational domain. For the numerical simulations a structured C-O coordinate mesh has been generated with the code IMESH [21], see Fig. 4.

In subsonic and transonic flow the grid covers a domain of 4 body lengths in all directions around the configuration. For Euler calculations about 600,000 grid points and for Navier-Stokes calculations about 900,000 grid points were used. In both cases the central differencing scheme with artificial dissipation was applied and viscous turbulent calculations have been carried out by means of the Baldwin-Lomax turbulence model [22] with the Degani-Schiff modification [23].

In supersonic flow the computational domain ended at the bow shock and at the trailing edge of the body. The number of grid points for Euler calculations was about 400,000. In these calculations the upwind flux vector splitting scheme has been used.

Concerning post processing, the aerodynamic forces and moments of the waverider configuration have been calculated by integration over the surface of the forebody. The base area has not been taken into account.

4.4 Windtunnel model

For the modified waverider configuration DLR–F8 a windtunnel model has been built. Its dimensions

$$l = 504.4 \, \text{mm}$$
$$b = 330.0 \, \text{mm}$$

allow investigations in the

0.4 m	Hypersonic Windtunnel of DLR Köln
$1 \times 1 \, \text{m}^2$	Transonic Windtunnel of DLR Göttingen
1.3 m	Low Speed Windtunnel of TU Braunschweig .

The model has sharp leading edges. In all windtunnels the model is fixed by a rear sting with the constant cross section of the nozzle area at the rear end of the model. This is the same geometry as used in the numerical simulations. In the experiments the base pressure in the nozzle area is measured by 4 pressure tabs. On this basis the contribution of the base area to the drag has been estimated and subtracted from the balance-measured drag in order to get the forebody drag for comparison with numerical results.

In all windtunnels forces and moments are measured by means of an internal strain gauge balance. In two cross sections

$$x/l = 0.29 : \qquad 0 \le y/y_1 \le 1$$
$$x/l = 0.75 : \qquad 0 \le y/y_1 \le 1$$

and one chordwise section at $y/s = -0.5$ the model is equipped with pressure tabs and an internal tube system which leaves the model through the nozzle area at the base. The sections with pressure tabs are shown in Fig. 3 and the distribution of some pressure taps may be taken from Fig. 16. The measurements in the 0.4 m Hypersonic Windtunnel are still in progress. In addition some flowfield studies have been carried out by means of surface oilflow investigations and for incompressible flow probe measurements have been performed. The experimental programs carried out in two windtunnels may be taken from Tab. 2.

5. Performance and flow characteristics in supersonic and hypersonic flow

The off-design behaviour of the described waveriders is given in Fig. 5 where L/D is plotted against the Mach number for $\alpha = 0°$. For inviscid flow around configuration WRE 12.0-IFL L/D is nearly Mach number independent as long as $M_\infty > 6.0$ because the leading edge is supersonic with an attached shock wave. For $M_\infty < 6.0$ L/D increases until it reaches a maximum at $M_\infty = 2.0$. The reason for this effect is that the shock wave detaches from the leading edge, if the sweep angle is sufficiently large, see Fig. 6. In regions with a detached shock wave an expansion around the leading edge appears. This expansion induces an additional lift but due to the fact that a free stream upper surface is considered no additional wave drag appears. At lower supersonic Mach numbers most of the leading edge is subsonic and flow separation from the leading edge occurs for $\alpha = 0°$.

4.

The resulting leading edge vortex creates additional suction and hence improves L/D again.

For inviscid flow around the configuration DLR–F8 the L/D values are lower compared to the waverider WRE 12.0–IFL with free stream upper surface according to Fig. 5. This is a result of the expansion flow region introduced along the rear part of the upper side which can be taken from Fig. 7. The lower surface is nearly unchanged and at design flow conditions ($M_\infty = 12.0$) the expansion on the upper surface induces additional lift (+7.7 %) and an increase of the wave drag (+9.6 %). This decreases $(L/D)_i$. Since the influence of the upper surface on the aerodynamic coefficients is stronger at lower Mach number, this effect increases with decreasing Mach number. In supersonic flow the additional lift resulting from the expansion around the leading edge and the vortices appear also for the waverider DLR–F8. Again, the additional vortex lift increases L/D. A description of the phenomena which cause the increase in lift may be taken from Fig. 7 and Fig. 8, where the surface streamlines and the pressure distributions are plotted. For $M_\infty = 6.0, \alpha = 0°$ (Fig. 7) the entire leading edges are supersonic and therefore, the streamlines are aligned with the free stream. The pressure distribution in the rear part of the body shows the influence of the expansion along the upper surface. In Fig. 8 similar plots are given for $M_\infty = 2.0, \alpha = 0°$. Along the leading edge the influence of a vortex is obvious due to the appearance of an attachment line. Considering the pressure distributions a vortex-induced suction region is found along the upper surface. The distributions show also the expansion flow region which is due to the modified upper surface. It is obvious that the influence of the upper surface increases with decreasing Mach number.

Another situation occurs if viscous effects are taken into account. According to Fig. 5 the waverider configuration WRE 12.0-IFL exhibits L/D values of about 7 for $M_\infty > 6.0$. Adding additional lift and drag at a ratio of about 7 : 1 does not degrade the overall L/D as shown in Fig. 5 for DLR–F8. Hence, it is demonstrated that the design of realistic waverider configurations with sharp trailing edges is possible without compromising L/D at hypersonic flow conditions, if skin friction is taken into account.

Concerning the design of realistic waverider shapes the effect of a blunt leading edge on the aerodynamic performance has to be considered. In the design point waverider shapes are always sharp–nosed, but leading edges of realistic designs have to be properly blunted in order to reduce the heat loads. On the other hand the chosen nose radius should be as small as possible for low wave drag. Results from Ref. [18] indicate that a nose radius of $r_N/l = 0.0001$ would be feasible for a configuration with l = 70 m. Then the decrease in L/D would be approximately 1.6 % and with regard to the expected numerical accuracy this effect is negligible. The application of such a small blunt-

ness requires technical solutions for the design of the leading edge and is important with respect to the realization of such an aircraft. The precise analysis of the structural design and the selection of a suitable material is expected to include the full thermal interactions between the fluid flow and the structure to get realistic results for the temperature distribution inside the leading edge. For that reason a numerical strategy for the coupling of a Navier-Stokes code for the flow analysis with a thermal code for the structural analysis was developed [24] and applied to investigate the thermal behaviour of the leading edge structure [25]. For aerodynamically sharp leading edges ($r_N < 10$ mm) under hypersonic conditions the resulting wall temperatures at the stagnation point are significantly smaller (about 200 - 300 K) than the wall temperatures calculated according to a local balance of radiation and aerodynamic heat flow on the wall. This reduction of the wall temperature is based on the heat conduction of the structure. It is reached without any additional active cooling. Therefore, the use of conventional materials with operational temperatures below 2000 K for the leading edge structure could be sufficient for the technical realisation. Further reduction of the maximum temperature could be obtained by an active cooling through small heat-pipes in the leading edge structure or by the variation of the aerodynamic shape for instance. More details concerning this subject are given in Ref. [24]. The numerical results show, that the thermal design problems of waveriders can be controlled.

6. Performance and flow characteristics in subsonic and transonic flow

Along the entire flight trajectory of a hypersonic waverider from incompressible flow at take-off up to hypersonic flow under cruise conditions the greatest changes with respect to flow characteristics and aerodynamic performance take place in the transonic regime. Careful attention has to be drawn to this flight regime since it may be dimensioning for the engine layout. Predesign studies [25] show that almost 25 % of the fuel for a hypersonic orbit transport mission is consumed between take-off and $M_\infty = 1.5$, the Mach number range which is discussed in this chapter.

The performance data of DLR–F8 in the considered speed regime are shown in Fig. 9 for an angle of attack of $\alpha \approx -1.0°$ and a Reynolds number of $Re_\infty \approx 6.5 \times 10^6$. Due to the definition of the angle of attack according to Fig. 3 and an angle between wing and body ridge line of approximately 5°, the zero-lift angle of attack of DLR-F8 in this speed regime is $\alpha_0 \approx -6.0°$. Hence, $\alpha = -1.0°$ corresponds to an effective angle of attack of about 5° , leading to realistic lift coefficients of hypersonic flight vehicles for transport missions in this Mach number range.

In supersonic flow the leading edge vortex expands only slightly with decreasing Mach number as illus-

5 .

trated in Fig. 10 by means of streamlines and pressure distributions on the upper surface of DLR–F8 at $M_\infty = 1.5$ and $M_\infty = 1.025$. At $M_\infty = 1.5$ the flow separates at the leading edge at $x/l \approx 0.06$. In the rear part, downstream of $x/l \approx 0.9$ a Prandtl-Meyer expansion around the leading edge occurs due to the lower leading edge sweep, shifting the separation line from the leading edge onto the upper surface. However, at $M_\infty = 1.025$ the onset of the leading edge separation moves slightly upstream ($x/l \approx 0.03$) and extends to the trailing edge in downstream direction. Due to the compressibility effects in supersonic flow the suction along the vortex axis increases with decreasing Mach number, and this produces higher suction forces on the contour and increases the lift. In addition the compressibility effects increase with decreasing leading edge sweep. Therefore, the suction peaks are observed in the rear part of the configuration and this leads to a rearward shift of the centre of pressure with decreasing Mach number.

The supersonic flowfield around the waverider configuration shows two oblique shocks attached to the sharp nose and the trailing edge. If the Mach number is reduced to the transonic regime the front shock disappears and the terminating shock starts moving in upstream direction and weakens. In this flow regime the waverider aerodynamics at small and medium angles of attack up to $\alpha = 10°$ are determined by the upstream shift of the terminating shock and by the leading edge vortex. Both flow patterns are illustrated in Fig. 11. Due to the disappearence of the front shock, the weakening of the terminating shock and the reduction of the supersonic region on the surface with decreasing Mach number the wavedrag decreases drastically. Although the drag decrease is accompanied by a reduction of the lift coefficient, the aerodynamic efficiency rises from $L/D \approx 7$ in supersonic flow up to $L/D \approx 9$ in transonic and subsonic flow. The lift decrease is another result of the behaviour of the terminating shock: Suction regions, located formerly upstream of the shock, are transformed into pressure regions downstream of the shock and this reduces the lift of the configuration. As a further consequence the contribution of the rear part of the waverider to the lift decreases and the centre of pressure moves upstream.

In transonic flow from $M_\infty = 0.85$ to $M_\infty = 1.05$ the Navier-Stokes results show good agreement with the experimental data. The differences between the lift coefficients are below 3 %, the maximum drag deviation is approximately 10 drag counts at $M_\infty = 0.85$ and the centre of pressure corresponds at a maximum deviation of 1% of the body length with the measurements. A comparison between the experiments and the Euler results shows larger differences. Along the entire Mach number range under consideration a higher lift is predicted with a maximum difference of $\Delta C_L = 0.022$ ($\approx 12\%$) at $M_\infty = 0.95$. This is due to the fact that viscous effects, in particular the

secondary separation, are not covered by the Euler equations. The consequences of the limited numerical model are illustrated in Fig. 12a, showing the contour pressure distribution in spanwise direction. Based on the missing displacement effect of the secondary vortex the leading edge vortex is located closer to both the upper surface and the leading edge. Therefore, a higher pressure peak below the vortex occurs closer to the leading edge, and this is responsible for the larger lift in inviscid flow. In addition the Euler solution predicts a higher drag. In viscous flow the shock-boundary layer interaction damps the influence of the shock on the contour pressure distribution. Furthermore, the displacement effect of the boundary layer decambers the contour of the body. Both effects are missing in the inviscid solution: A stronger shock is predicted slightly closer to the trailing edge, see Fig. 12b, causing a higher wavedrag. However, the viscous part of the drag, which was calculated on the basis of the skin friction drag of a flat plate in turbulent flow, corresponds very well with the Navier-Stokes results, as indicated in Fig. 5. For the angle of attack, Mach numbers and Reynolds numbers under consideration, the viscous drag has with $C_{D,f} \approx 0.0065$ a share of approximately one third of the total drag. Coupling lift and drag in the aerodynamic efficiency, the flaws of the inviscid simulations compensate each other and lead to a result comparable to the Navier-Stokes solutions. Finally, in spite of the missing simulation of the secondary vortex, the Euler solution predicts the centre of pressure even closer to the experiment than the Navier-Stokes results. This indicates, that the development of the vortex flow in downstream direction is correctly predicted in inviscid flow.

A further reduction of the Mach number from $M_\infty = 0.8$ down to $M_\infty = 0.3$ is coupled with a slight decrease of L/D based on a decreasing lift coefficient at constant drag. The compressibility effects in subsonic flow are quite moderate due to the high leading edge sweep. However, in the rear part of DLR–F8, where the local sweep angle increases, a significant reduction of the suction especially below the leading edge vortex occurs. A comparison of the surface pressure distribution and streamlines between both Mach numbers $M_\infty = 0.8$ and $M_\infty = 0.3$ is given in Fig. 13. Fig. 14 shows the accompanying load distribution in longitudinal direction. The reduced lift contribution of the rear part at $M_\infty = 0.3$ is clearly indicated and is responsible for the noseward shift of the centre of pressure with decreasing Mach number in subsonic flow.

7. Performance and flow characteristics in incompressible flow

The investigations of the modified waverider configuration DLR-F8 in incompressible flow have been performed experimentally and numerically. The mea-

surements, see Tab. 2, have been carried out in the 1.3 m windtunnel of the Institute of Fluid Mechanics of TU Braunschweig. The numerical investigations have been performed with the DLR Euler/Navier-Stokes code FLOWER [20]. The comparison between experiments and numerical solution is shown subsequently for an angle of attack $\alpha = 12.2°$.

7.1 Aerodynamic forces and pitching moment

The results of the three-component measurements are given in Fig. 15. The well-known nonlinear dependence of the aerodynamic coefficients on the angle of attack for slender configurations at small and medium angles of attack turns out. For angles of attack $\alpha > 18.0°$ vortex breakdown takes place over the wing and lift, drag and nose–down pitching moment are reduced as indicated in Fig. 15 by hatching.

The numerical investigation has been performed with the Navier–Stokes code FLOWER for $\alpha = 12.2°$ with turbulent boundary layer using the Baldwin–Lomax turbulence model with the Degani–Schiff modification [22], [23]. The result is given in Fig. 15 by the filled symbols. Compared with the experiments the prediction of lift is reasonable whereas the drag coefficient C_D and the pitching moment coefficient C_{m25} differ considerably from the experimental results. The reasons for these discrepancies are discussed subsequently.

7.2 Surface pressure distribution

The surface pressure distribution in the two cross sections at $x/l = 0.29$ and $x/l = 0.75$ are given in Fig. 16 for the angle of attack $\alpha = 12.2°$. The pressure coefficient $-C_p$ is plotted against the dimensionless spanwise coordinate y/y_1 in the upper part and the corresponding cross section areas are shown below. In addition the pressure distribution in the cross section at $x/l = 0.75$ is also given with respect to the dimensionless coordinate z/y_1 on the lower right hand side of Fig. 16. The measured pressure distributions are marked by circles connected by a thin solid cubic spline curve and the locations of the pressure tabs are shown for each cross section by triangles. The Navier–Stokes results are given by the thick solid lines.

In both sections the suction peak due to the leading edge vortex is clearly indicated. In the front part at $x/l = 0.29$ the Navier–Stokes solution predicts higher suction due to the primary vortex and lower suction due to the secondary vortex. This means that the secondary vortex predicted by the numerical calculation is too small and the corresponding primary vortex is located closer to the wing surface as compared with the experiments. In the rear part of the configuration, however, the Navier–Stokes solution leads to a lower suction peak below the primary vortex. A detailed analysis shows differences in the size of the secondary vortex as well as of the strength of the primary vortex.

In the cross section $x/l = 0.75$ high suction occurs at the upper edge of the fuselage and flow separation takes place in its vicinity. Close to the sidewall of the fuselage a vortex is formed which produces additional suction indicated in Fig. 16 by hatching. This fuselage vortex is predicted by the Navier–Stokes calculation, but certain differences are observed concerning both the magnitude of the suction peak at the fuselage edge and the pressure distribution on the sidewall and on the wing.

The comparison between the Navier–Stokes solution and the experiments indicates that the turbulence model used in the present calculation does not predict all flow phenomena correctly. In addition the numerical results for the section $x/l = 0.75$ may also be effected to some extent by the grid resolution of the flowfield. Both effects lead to some differences between theory and experiment concerning size and strength of the primary, the secondary and the fuselage vortex, and this is assumed to be the reason for the differences in the pressure distribution according to Fig. 16b and in the aerodynamic coefficients according to Fig. 15.

7.3 Flowfield investigations

Since conventional five–hole probe technique was used the measurements had to be restricted to flowfields without vortex breakdown. As indicated in Fig. 15 vortex breakdown is present over the configuration for $\alpha > 18.0°$. In order to avoid artificial vortex breakdown caused by the probe the flowfield measurements have been carried out at an angle of attack $\alpha = 12.2°$ in three cross sections at

$$x/l = 0.29, 0.75, 1.01,$$

and for this case the Navier–Stokes solution with turbulent boundary layer has been performed. The results are shown in Fig. 17 by means of lines of constant total pressure coefficient C_g. The results of the Navier–Stokes calculation are also drawn for comparison. Concerning all three cross sections the large total pressure loss region in the outer portion of the wing is due to the leading edge vortex. This vortex is accompanied by a secondary vortex which is due to secondary flow separation below the leading edge vortex. These characteristics of the flowfield over the waverider configuration are well–known from slender delta wings. They are well predicted by the Navier–Stokes solution. However, there are some differences in shape, location and strength of both vortices especially in the cross sections at $x/l = 0.75$ and $x/l = 1.01$. In the plane $x/l = 0.29$ the strength of the primary vortex is well predicted by the numerical calculation, but the location of the secondary separation point is different and the calculated secondary vortex is too small. The same is true for the cross section at $x/l = 0.75$, and at $x/l = 1.01$ a secondary separation is no longer prescribed by the numerical solution.

This fact indicates that in the present calculation the grid was too coarse in the rear part of the flowfield. In the cross section at $x/l = 1.01$ the experiments show a deformation of the vortex sheet which is due to a tip vortex emanating from the kink between the swept leading edge and the side edge at $x/l = 0.95$ [26]. In this region the Navier–Stokes solution shows a rather wide vortex sheet, but a tip vortex cannot be observed. Numerical viscosity in combination with the coarse grid in the rear part of the flowfield may be the reason for these differences between theory and experiment.

In the cross sections at $x/l = 0.75$ and $x/l = 1.01$ the fuselage vortex is well documented in the experimental results as well as in the numerical solution. In more detail there are some differences in shape and strength of this vortex which again may be due to the grid resolution and the turbulence model. In conclusion the interference effects of the secondary vortex and the fuselage vortex on the primary vortex are slightly different in theory and experiment and this leads to the results for the pressure distribution discussed earlier.

Fig. 18 shows lines of constant local dynamic pressure in the plane $x/l = 0.29$. Concerning the experimental result there is a region of low dynamic pressure in the centre of the primary vortex which is surrounded by a region with high dynamic pressure having local maxima below and above the vortex axis. This distribution of dynamic pressure is similar to that found by Hummel [27] related to vortex breakdown, but intensive studies by laser light sheet technique have shown that in the present case no vortex breakdown takes place. This phenomenon can be explained as a planform effect in the front part of the waverider: The flow separation at the sharp leading edge starts in the symmetry plane similar to the 2D separation on an inclined flat plate. A separated flow region with a deadwater–type structure and low local dynamic pressures is established there. With increasing spanwise distance from the symmetry plane the sweep of the leading edge increases rapidly. Therefore a 3D flow separation takes place and the initial region of low dynamic pressure is surrounded by a vortical flow with increasing velocity towards the vortex centre. The axis of this vortex follows the leading edge and with increasing distance from the symmetry plane the velocity component parallel to the vortex axis increases. The velocity distribution in the vicinity of the vortex centre found in the section $x/l = 0.29$ of the waverider is an effect of the upstream leading edge curvature. It is distinctly different from that in the vortex over a delta wing which shows increasing velocity towards the vortex axis everywhere. The Navier–Stokes calculation predicts this distribution of dynamic pressure very well. Further studies of this phenomenon in various cross sections are in progress.

Fig. 19 shows the surface oilflow patterns for the angle of attack $\alpha = 12.2°$ and the corresponding surface streamlines from the solution of the Navier–Stokes equations. In the plan view of the oilflow picture a primary attachment line can be distinguished. In the front part of the waverider the attachment line follows the leading edge and more downstream it approaches the waverider symmetry line. Close to the leading edge a secondary separation line is observed which moves outboard at approximately 79 % rootchord position. This does not necessarily mean that transition from laminar to turbulent boundary layer is the reason for this, since there is a kink on the wing surface which could also cause an outboard shift of the secondary separation line. From this point of view further studies of the boundary layer are necessary. Towards the fuselage an attachment line can be distinguished on the wing surface which is related to the fuselage vortex. Considering the side view of the surface oilflow patterns the corresponding separation line can be distinguished in the vicinity of the upper fuselage corner. Towards the wing surface another separation line can be observed which is due to a secondary fuselage vortex.

The mean characteristics of the flow around the waverider are well predicted by the Navier–Stokes solution. However, the position of both the attachment line due to the primary vortex and the secondary separation line differ from the experiment, and in the rear part the secondary separation is not predicted correctly. These differences are due to the influence of the numerical viscosity and the coarse grid in the rear part of the configuration. In addition the turbulence model which is used in the present calculation affects the numerical solution. Concerning the fuselage vortex the separation and the attachment line are well predicted as shown in the side view and plan view of Fig. 19, but a secondary separation line on the sidewall cannot be observed. This discrepancy in comparison to the experiment is also due to the turbulence model applied in the present study.

8. Conclusions

The waverider configuration DLR–F8 has been generated at $M_\infty^\star = 12.0$ using the interactive code WIPAR for the lower surface and an expansion surface has been designed for the upper surface. This geometry has been investigated in the whole Mach number range both experimentally and numerically. Numerical codes for the solutions of the Euler and the Navier–Stokes equations turned out to be powerful tools for the description of the performance characteristics and of the details of the flowfield.

The design of the configuration well above the cruise Mach number led to practicable distributions of camber and volume. The performance characteristics remained constant on a very high level for decreasing Mach number. If the shock wave detaches from the leading edge L/D increases considerably for both supersonic and subsonic leading edges due to the expansion flow and the leading edge vortex formation

on the upper surface. The leading edge bluntness can be chosen very small to avoid a significant increase of wave drag, and the corresponding thermal loading can be overcome by a proper combination of material and structural design.

The highest values for L/D are achieved in the transonic flow regime. The flow is still governed by leading edge vortices, but considerable changes in the centre of pressure position are due to movements of the terminating shock location. The compressibility effects are well predicted by the Euler solutions and the estimation of the viscous drag by means of flat plate results has been validated by Navier–Stokes calculations.

The flow studies in the incompressible flow regime showed the well–known primary and secondary vortices over the wing and a fuselage vortex at the sidewall of the configuration. The structure of the primary vortex is different from that on delta wings: In the vortex centre a region of reduced velocity is present which is due to the leading–edge curvature in the front part of the waverider. These flow phenomena are very well predicted by corresponding Navier–Stokes calculations.

9. References

[1] Nonweiler, T.R.F.: Aerodynamic problems of manned space vehicles. J. Roy. Aeron. Soc. 63 (1959), 521-528.

[2] Rasmussen, M. L.: Waverider configurations derived from inclined circular and elliptic cones. J. Spacecraft Rockets 17 (1980), 537-545.

[3] Bowcutt, K.G., Anderson, J.D. Jr., Capriotti, D.: Numerical optimization of conical flow waveriders including detailed viscous effects. AGARD CP-428 (1987), 27-1 to 27-23.

[4] Corda, S., Anderson, J.D. Jr.: Viscous optimized waveriders designed from axisymmetric flowfields. AIAA Paper 88-0369 (1988).

[5] Sobieczky, H., Dougherty, F.C., Jones, K.D.: Hypersonic waverider design for given shock waves. Proceedings of the 1st Internat. Hypersonic Waverider Symposium 1990, University of Maryland.

[6] Center, K.B., Jones, K.D., Dougherty, F.C., Sebass, A.R., Sobieczky, H.: Interactive hypersonic waverider design and optimization. Proc. 18th ICAS Congress Beijing 1992, Vol. 2, 1571-1580.

[7] Radespiel, R., Eggers, Th., Strohmeyer, D., Körner, H., Heinze, W., Bardenhagen, A., Kossira, H., Hummel, D.: Entwurf von Wellenreitern für Hyperschallflugzeuge. DLR-Nachrichten 80 (1995), 2-10.

[8] Eggers, Th., Sobieczky, H., Center, K.B.: Design of advanced waveriders with high aerodynamic efficiency. AIAA Paper 93-5141 (1993).

[9] Eggers, Th., Radespiel, R.: Design of waveriders. Space Course TU München 1993, 6-1 to 6-39.

[10] Kossira, H., Bardenhagen, A., Heinze, W.: Investigation on the potential of hypersonic waveriders with the integrated aircraft design program PrADO-Hy. AIAA Paper 93-5161 (1993).

[11] Bardenhagen, A., Kossira, H., Heinze, W.: Interdisciplinary design of modern hypersonic waveriders using the integrated program PrADO-Hy. Proc. 19th ICAS Congress Anaheim 1994, Vol. 2, 1053-1063.

[12] Rossow, C.–C.: Berechnung von Strömungsfeldern durch Lösung der Euler-Gleichungen mit einer erweiterten Finite-Volumen Diskretisierungsmethode. Dissertation TU Braunschweig 1988. DLR-FB 89-38 (1989).

[13] Radespiel, R., Kroll, N.: Accurate flux vector splitting for shocks and shear layers. J. Comput. Physics 121 (1995), 66–78.

[14] Eggers, Th., Radespiel, R., Waibel, M., Hummel, D.: Flow phenomena of hypersonic waveriders and validation of design methods. AIAA Paper 93-5045 (1993).

[15] Eggers,Th.: Vorentwurf von Hyperschallkonfigurationen mit der Stoß-Expansions-Methode SOSE. 8. DGLR-Fach-Symposium, 1992, DGLR–Bericht 92–07, 295–304.

[16] Eggers, Th.: Untersuchungen zum Off-Design-Verhalten von Wellenreitern im Überschallbereich. DGLR Jahrbuch 1994, Bd. 2, 725–734.

[17] Strohmeyer, D., Longo, J.M.A.: Aerodynamische Untersuchung einer Wellenreiterkonfiguration im Unter- und Transschall. 9. DGLR-Fach–Symposium 1994, DGLR–Bericht 94–04, 191–196.

[18] Eggers, Th., Strohmeyer, D., Nickel, H., Radespiel, R.: Aerodynamic off-design behavior of integrated waveriders from take-off up to hypersonic flight. AIAA Paper 95-6091 (1995).

[19] Eggers, Th., Strohmeyer, D.: Design of high L/D vehicles based on hypersonic waveriders. AGARD Conference "Future Aerospace Technology in the Service of the Alliance" Paris 1997, Paper C-18 (1997).

[20] Kroll, N., Rossow, C.–C., Becker, K., Thiele, F.: MEGAFLOW - A numerical flow simulation system. 21st ICAS Congress 1998, Melbourne, Paper 2.7.4 (1998).

[21] Herrmann, U.: IMESH - An interactive mesh generation package for graphics super workstations. 3rd Internat. Conf. on Numer. Grid Generation in CFD and Related Fields, Barcelona, Spain 1991.

[22] Baldwin, B.S., Lomax, H.: Thin layer approximation and algebraic model for separated turbulent flows. AIAA Paper 78-275 (1978).

[23] Degani, D., Schiff, L.B.: Computation of turbulent supersonic flows around pointed bodies having crossflow separation. J. Comput. Physics 66 (1988), 173-196.

9

[24] Haupt, M., Kossira, H., Radespiel, R.: Analyse von aerothermodynamisch belasteten Flügelvorderkanten mit einer Methode der Fluid-Struktur-Kopplung. DGLR Jahrbuch 1995, Bd. 3, S. 1429 - 1438.

[25] Strohmeyer, D., Eggers, Th., Heinze, W., Bardenhagen, A.: Planform effects on the aerodynamics of waveriders for TSTO missions. AIAA Paper 96-4544 (1996).

[26] Hummel, D., Oelker, H.-Chr.: Low–speed characteristics for the wing–canard configuration of the international vortex flow experiment. J. Aircraft 31 (1994), 868-878.

[27] Hummel, D.: Documentation of separated flows for computational fluid dynamics validation. AGARD CP-437 (1988), Vol. 2, P 15-1 to P 15-24.
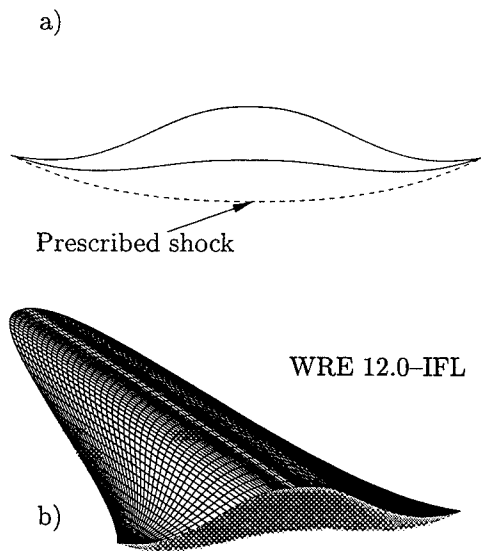
Fig. 1: Basic waverider design WRE 12.0-IFL. $M_\infty^* = 12.0, \sigma = 9.1°$, free stream upper surface.
a) Cross section at $x/l = 1$
b) View of the waverider from above
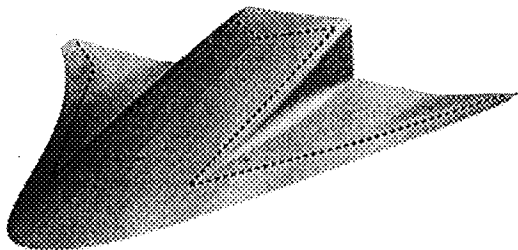
Fig. 2: Waverider configuration DLR-F8. (View from above)
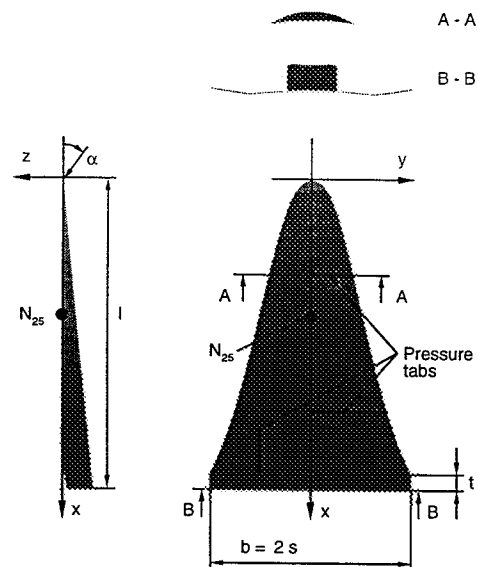
Fig. 3 Coordinate system.
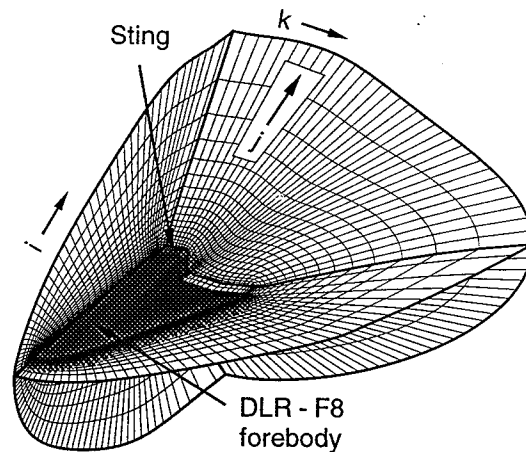
Fig. 4: Inner portion of the structured C–O mesh for the waverider DLR–F8.

10.
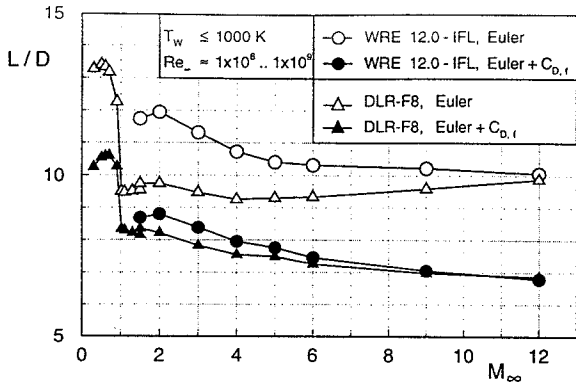
Fig. 5: Mach number influence on aerodynamic
efficiency at $\alpha = 0°$ for WRE 12.0–IFL
and DLR–F8. ($C_{D,f}$ friction drag accord-
ing to Reynolds numbers related to a re-
alistic trajectory [25])
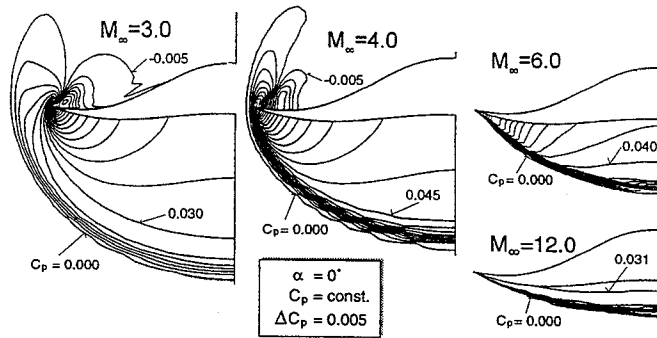
Fig. 6: Mach number effect on flowfield in the
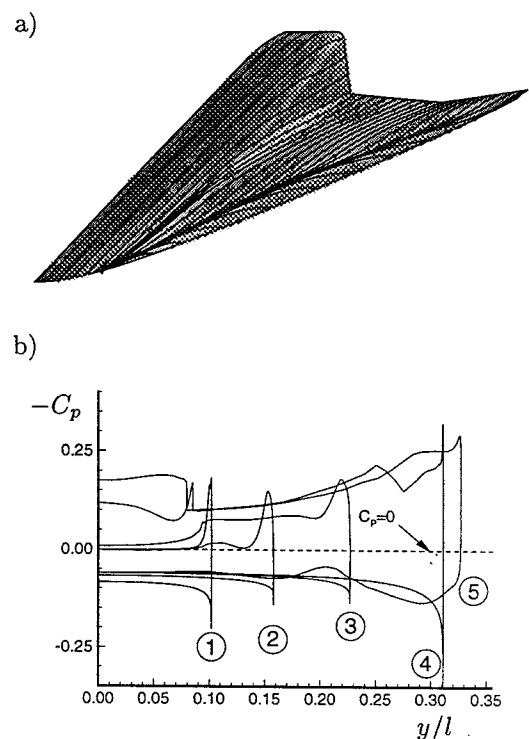cross section $x/l = 1.0$ according to
Euler calculations.
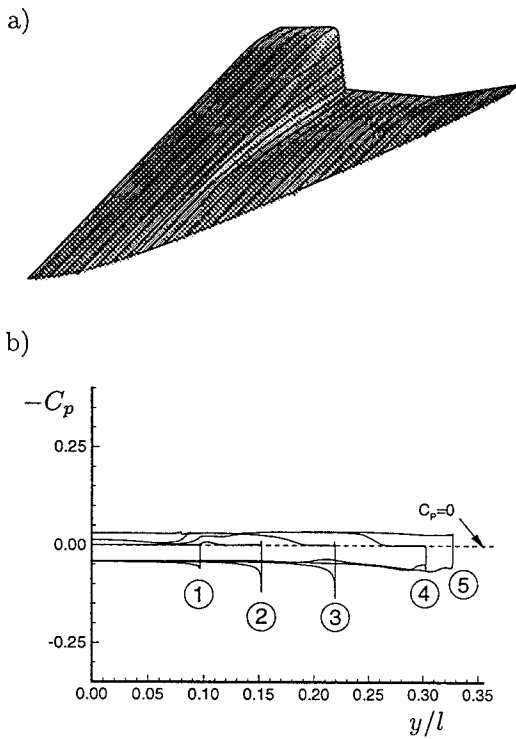
Fig. 7: Surface flow on configuration DLR–F8
according to Euler calculations for
$M_\infty = 6.0$ and $\alpha = 0°$,
a) Streamlines
b) Pressure distribution (sections)
c) Pressure distribution (upper surface)

Fig. 8: Surface flow on configuration DLR–F8
according to Euler calculations for
$M_\infty = 2.0$ and $\alpha = 0°$.
a) Streamlines
b) Pressure distribution (sections)
c) Pressure distribution (upper surface)
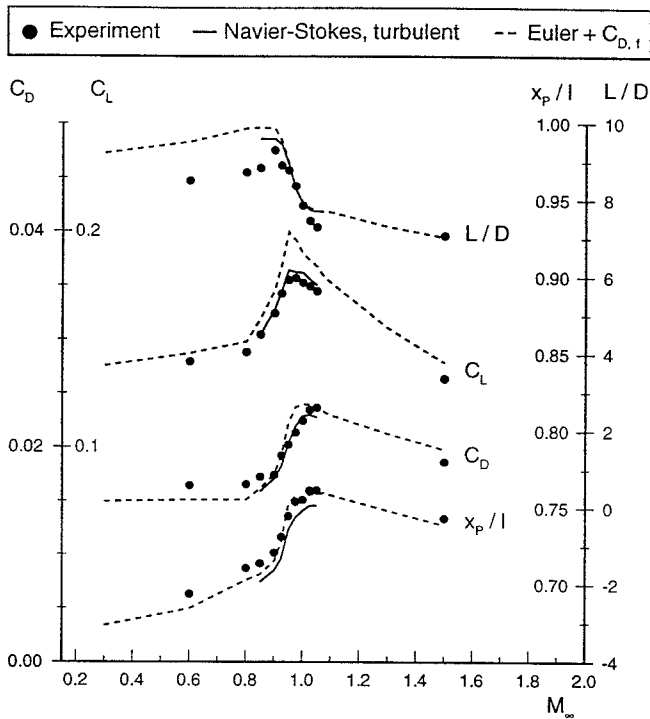
Fig. 9: Performance data of DLR–F8 in subsonic and transonic flow. Comparison of Euler– and Navier–Stokes calculations with measurements for $\alpha \approx -1.0°$ and $Re_\infty \approx 6.5 \times 10^6$.
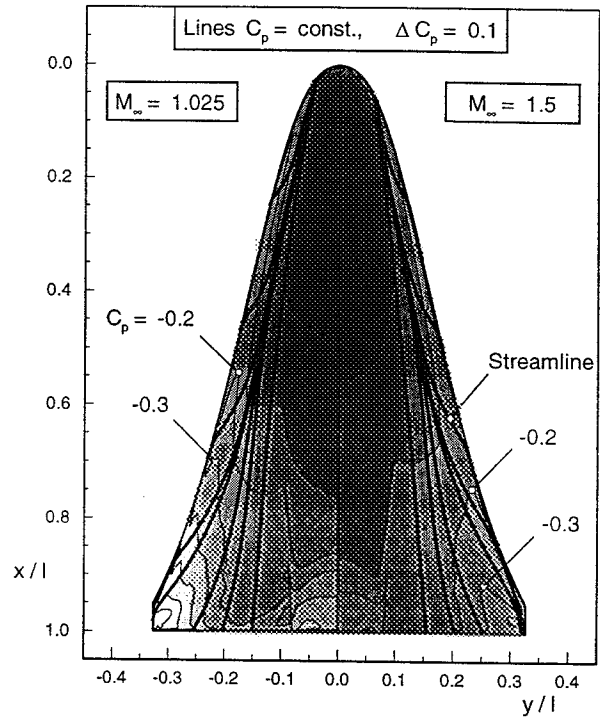
Fig. 10: Upper surface streamlines and pressure distributions on DLR–F8 in supersonic flow according to Euler calculations for $\alpha = 0°$.
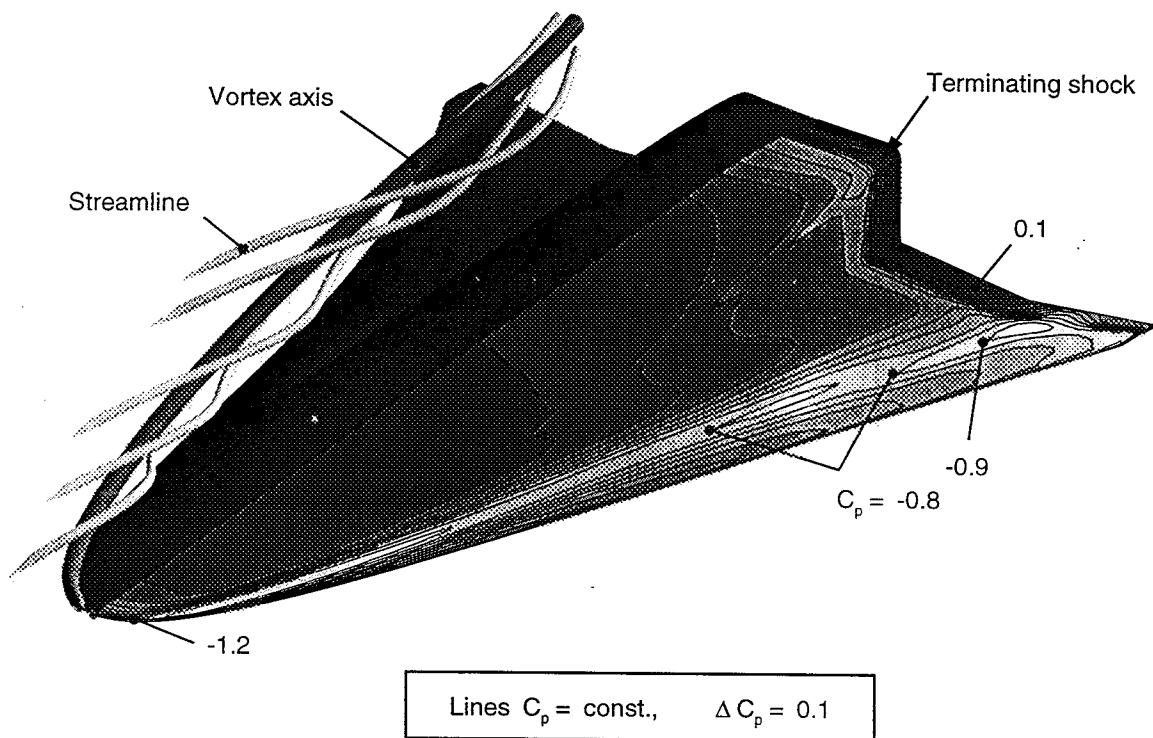
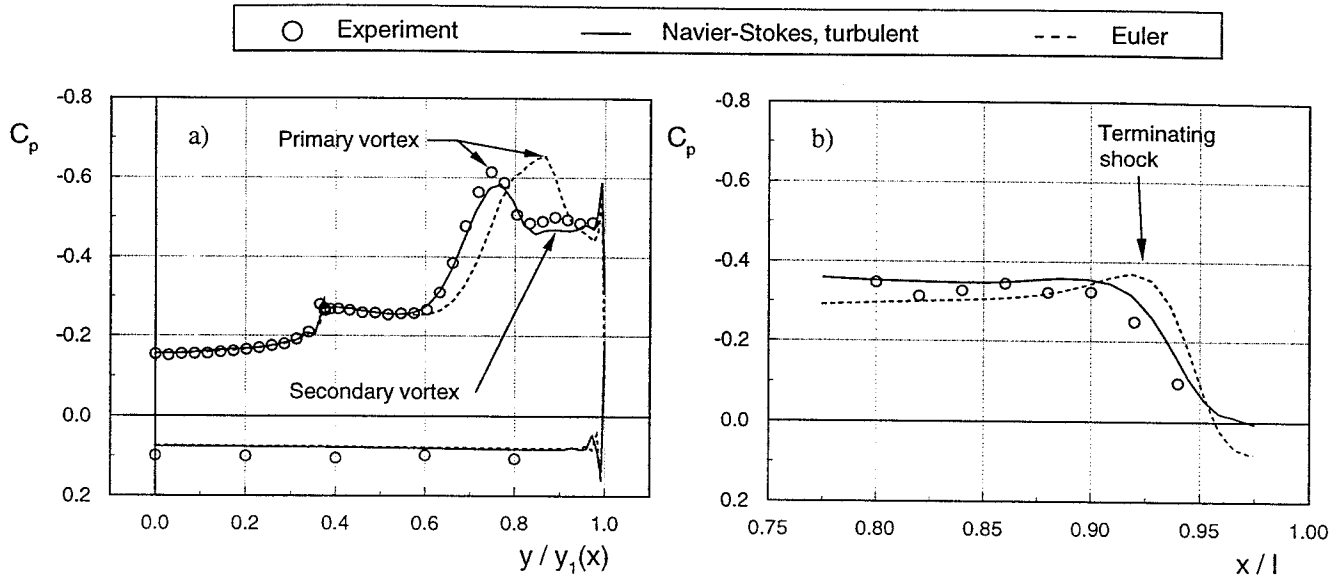Fig. 11: Vortex formation and surface pressure distribution on the DLR–F8 configuration according to Euler calculations for $\alpha = 5.0°$ and $M_\infty = 0.9$.

○ Experiment ———— Navier-Stokes, turbulent - - - Euler

Fig. 12: Pressure distribution on waverider DLR–F8
a) in the cross section at $x/l = 0.75$
b) in the longitudinal section at $y/s = -0.50$.
Comparison between theory and experiment for $\alpha = 2.95°$, $M_\infty = 0.9$ and $Re_\infty = 4.4 \times 10^6$.

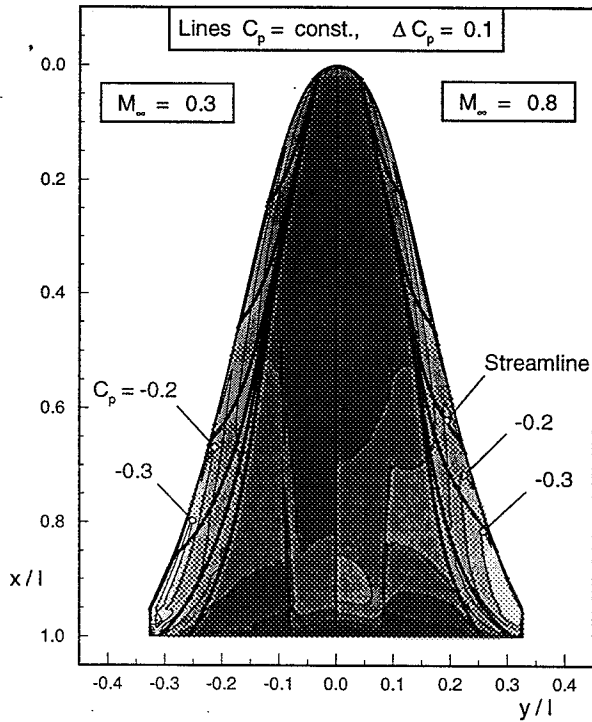Fig. 13: Upper surface streamlines and pressure
distributions on DLR–F8 in subsonic flow
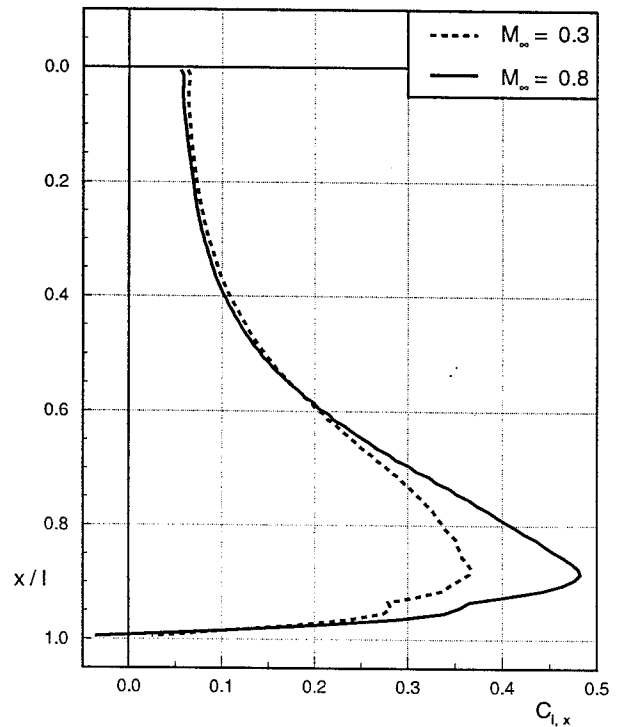according to Euler calculations for
$\alpha = 0°$.

Fig. 14: Distribution of cross–sectional local lift
in longitudinal direction of DLR–F8 in
subsonic flow according to Euler
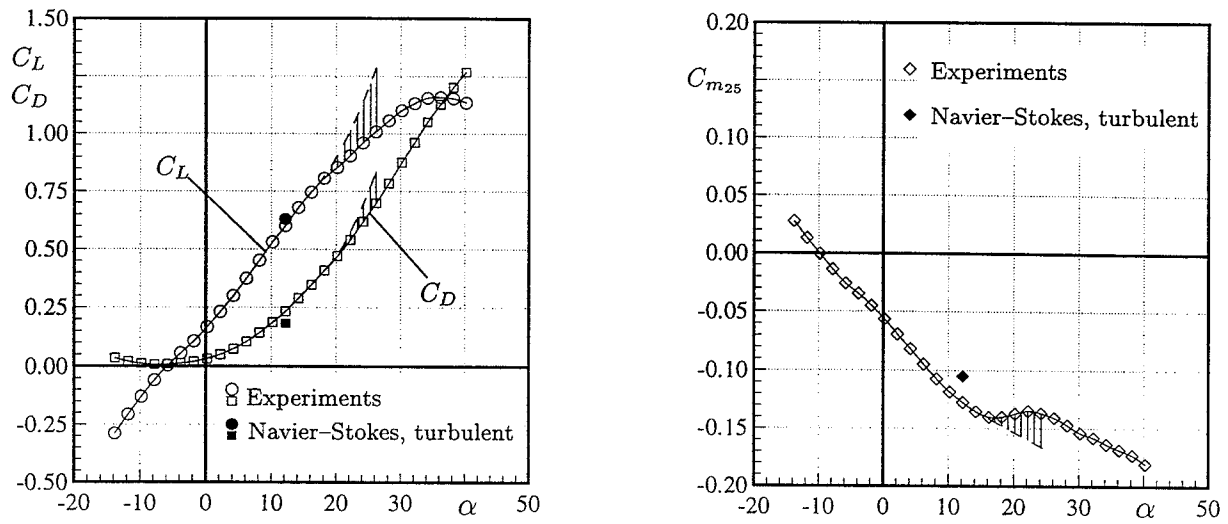calculations for $\alpha = 0°$.

13.

Fig. 15: Lift, drag and pitching moment characteristics for the waverider DLR–F8 at $M_\infty = 0.1$ and $Re_\infty = 1 \times 10^6$. (Effect of vortex breakdown marked by hatching)
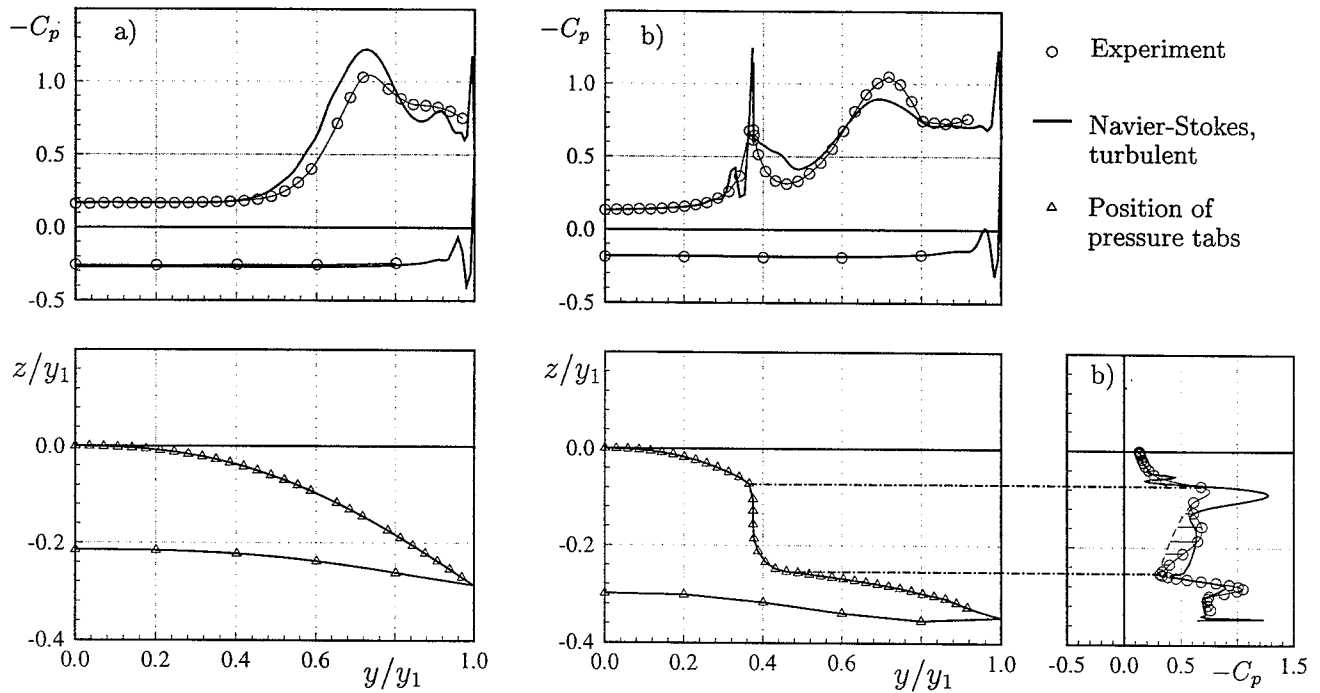
Fig. 16: Pressure distribution on the waverider DLR–F8 at $\alpha = 12.2°$ and $Re_\infty = 1 \times 10^6$
a) in the cross section at $x/l = 0.29$
b) in the cross section at $x/l = 0.75$.
Comparison of Navier–Stokes calculation at $M_\infty = 0.3$ with experiment at $M_\infty = 0.1$.
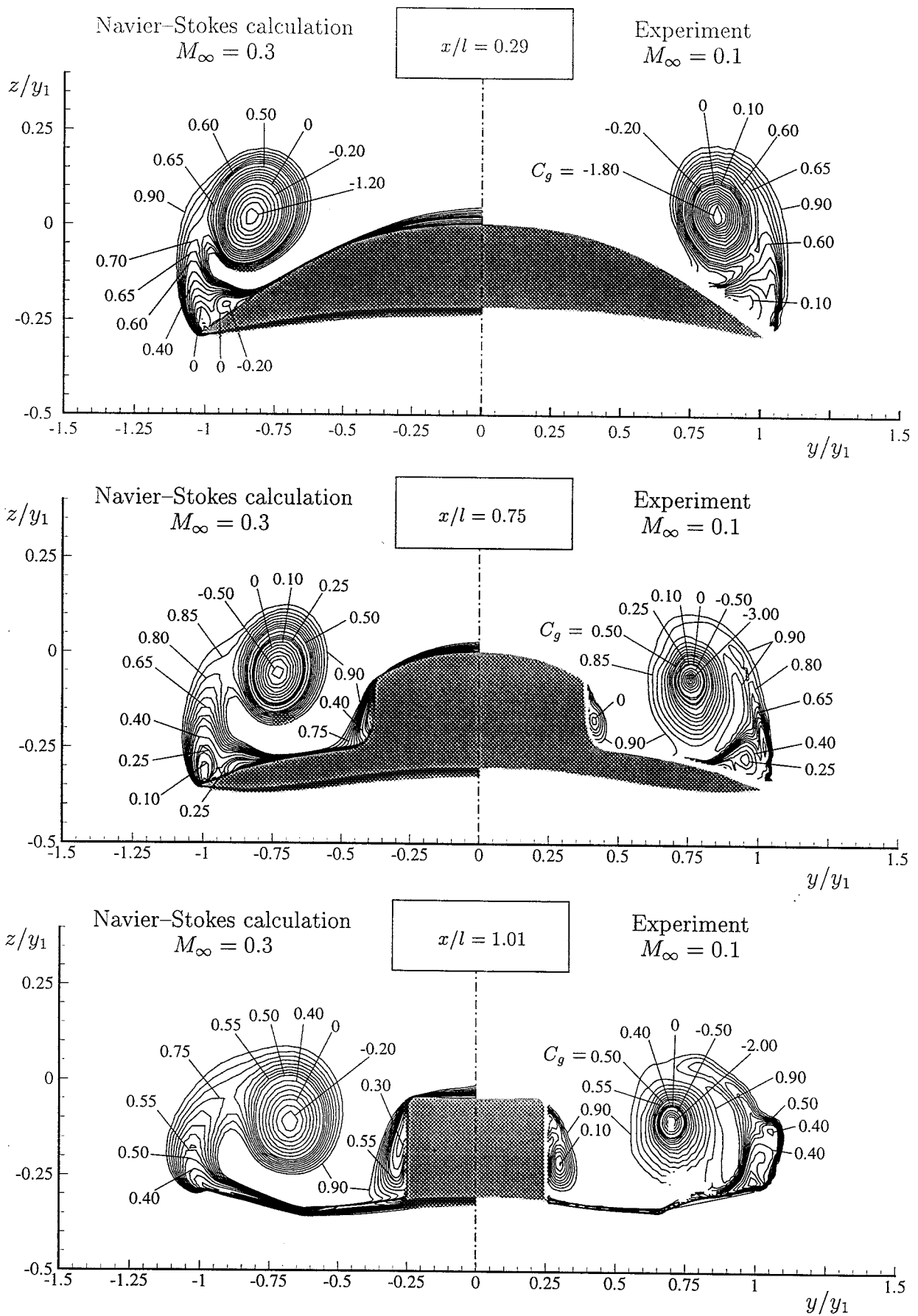(Effect of fuselage vortex marked by hatching)

14.

Hummel, Bloschke et. al.

Fig. 17: Flowfield on the waverider configuration DLR–F8 at $\alpha = 12.2°$ and $Re_\infty = 1.0 \times 10^6$ in different cross sections. (Lines of constant total pressure coefficient $C_g = (g - p_\infty)/q_\infty = \text{const.}$)
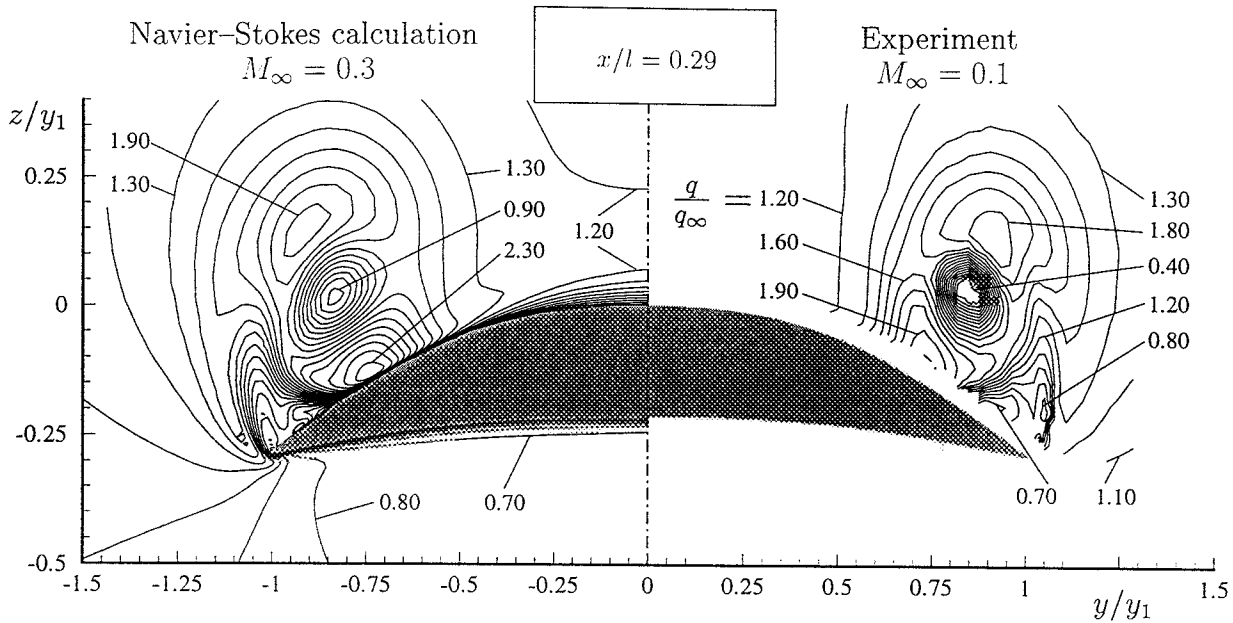
15.

Fig. 18: Flowfield on the waverider configuration DLR–F8 at $\alpha = 12.2°$ and $Re_\infty = 1.0 \times 10^6$ in the cross section at $x/l = 0.29$. (Lines of constant dynamic pressure $q/q_\infty = $ const.)
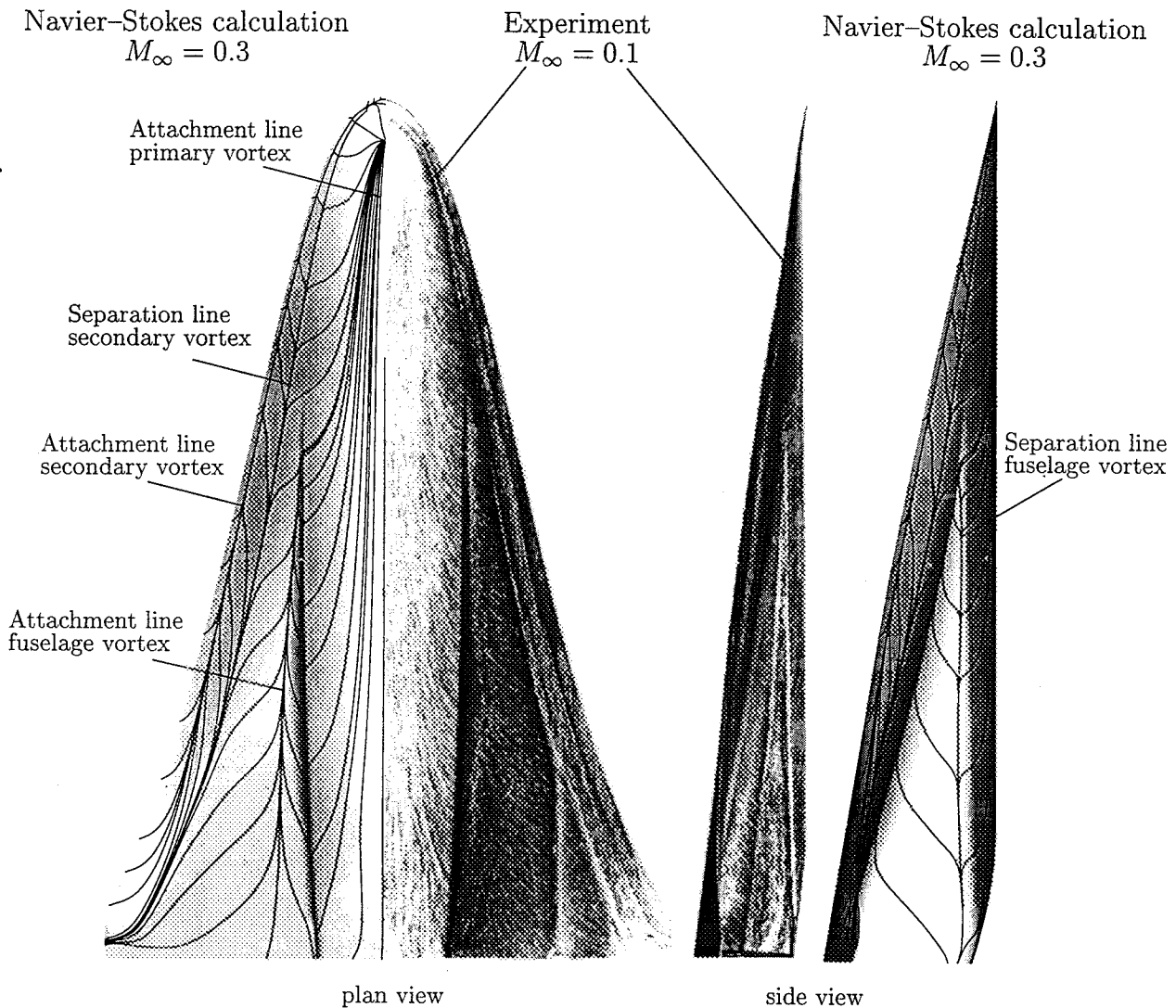

Fig. 19: Upper surface streamlines on the waverider configuration DLR–F8 at $\alpha = 12.2°$ and $Re_\infty = 1.0 \times 10^6$. Comparison between the results of Navier–Stokes calculation and experimental oilflow patterns. (In the case of the Navier–Stokes calculation, the fuselage is enlarged about 80 % in the side view)

		a) Basic configuration WRE 12.0-IFL	b) Modified configuration DLR–F8
Mach number	M_∞^*	12.0	12.0
Shock angle	σ	9.1°	9.1°
Aspect ratio	A	1.35	1.15
Volumetric efficiency	η	0.152	0.126
Centre of gravity position	x_{CG}/l	0.72	0.67
Geometric neutral point position	$x_{N_{25}}/l$	0.44	0.44
Angle of attack	α	0°	0°
Lift to Drag ratio inviscid flow	$(L/D)_i$	10.21	9.81
viscous flow	$(L/D)_v$	6.97	6.96
Centre of pressure position	x_P/l	0.63	0.64
Aerodynamic centre position	x_N/l	0.63	0.61

Tab. 1: Geometric data and aerodynamic characteristics of the two waverider configurations at $M_\infty^* = 12.0$ according to the design code WIPAR (a) and the Navier–Stokes code CEVCATS (b).

Windtunnel	$1 \times 1\,\mathrm{m}^2$ Transonic Windtunnel DLR Göttingen (TWG)	1.3 m Low Speed Windtunnel TU Braunschweig
Mach number range	$0.6 \div 2.0$	0.1
Reynolds number	6.5×10^6	1.0×10^6
Angle of attack range	$-7° \div 7°$	$-14° \div 40°$
Angle of sideslip range	0°	$-20° \div 25°$
Scope of experimental investigations	3-component balance measurements	6-component balance measurements
	Pressure distributions C_p	Pressure distributions C_p
		Flowfield measurement by probe
		Flowfield investigations by laser lightsheets
	Surface oilflow visualization documented by video	Surface oilflow visualization documented by photo

Tab. 2: Investigations on the waverider configuration DLR–F8 in different windtunnels.

Hummel, Plaschke et. al.